BULLETIN OF THE POLISH ACADEMY OF SCIENCES
TECHNICAL SCIENCES, Vol. 74(2), 2026, Article number: e157329
DOI: 10.24425/bpasts.2026.157329

Projectile shape optimization using numerical twin with computational fluid dynamics and design of experiment methods

Krzysztof PIASTA* and **Radosław TRĘBIŃSKI**

Jarosław Dąbrowski Military University of Technology, ul. Kaliskiego 2, 00-908 Warsaw, Poland

Abstract. Projectile shape optimization is crucial for enhancing aerodynamic performance and cost-effectiveness in ammunition development. This paper presents an integrated methodology leveraging the numerical twin concept, combining computational fluid dynamics (CFD) with design of experiments (DOE) methods to optimize projectile external geometry. The CFD model, serving as the core of the numerical twin, enables accurate prediction of the aerodynamic drag coefficient, validated against experimental data with a deviation of less than 6.5% at Mach 2.73. A structured experimental plan was established to determine the relationship between key geometric parameters and the drag coefficient for Mach numbers ranging from 2 to 2.75. Based on these results, a response function approximating the drag coefficient was formulated and integrated into the trajectory model, showing agreement with PRODAS software (less than 1.26% difference in terminal velocity and range). A second DOE plan was then used to optimize the shape of a prospective projectile for maximum terminal velocity at 300 meters, achieving 753 m/s. The resulting optimization tool provides time-effective estimations of terminal ballistics improvement for slight geometrical modifications. This holistic CFD-DOE approach streamlines and reduces the cost of projectile shape optimization, lessening the need for extensive prototyping and accelerating the design cycle.

Keywords: external ballistics; numerical twin; computational fluid dynamics; design of experiments; shape optimization; trajectory modeling.

1. INTRODUCTION

The design of experiments (DOE) methodology was developed to analyze how multiple factors affect a given object – whether a product or a process – and how these factors influence the resulting characteristics of that object, known as the response. The DOE methodology applies to five categories of experimental problems: treatment comparison, variable screening, response surface exploration, system optimization, and system robustness [1]. These same categories are relevant to numerical experiments, where a numerical twin replaces the physical object. Numerical twin is a computational representation that replicates the essential physical behavior of a real-world object or system with sufficient fidelity to enable simulation, analysis, and prediction of its performance under specified conditions. In this context, the numerical twin acts as a measurement tool, and each simulation run can be interpreted as a single measurement. DOE is particularly valuable in the optimization of technical systems through the optimization of their numerical twins.

Computational fluid dynamics (CFD) is the principal tool used to construct and operate the numerical twin. CFD solves the governing equations of fluid flow around any geometry, enabling estimation of aerodynamic forces and moments under controlled conditions. Integrating CFD with DOE allows for the exploration of how geometric parameters and flight conditions interact to influence aerodynamic characteristics and the efficient identification of optimal configurations.

The motivation for this study stems from the need to improve the aerodynamic performance of small-arms projectiles, where incremental reductions in drag can lead to meaningful gains in impact velocity and effective range. While prior research provided extensive insights into the influence of projectile geometry on drag [2, 3], most of the findings often rely on one-factor-at-a-time testing or semi-empirical methods that can overlook interactions between variables. This work addresses this gap by applying a structured DOE approach to systematically model and optimize projectile geometry using validated CFD simulations.

In this study, a numerical twin of a small-arms projectile was developed by constructing a CFD model capable of accurately estimating aerodynamic drag across a range of Mach numbers (Ma) and geometric variations. Methods from response surface exploration and system optimization were employed to derive a predictive model of drag coefficient behavior, which is an objective function describing the dependence of the aerodynamic drag coefficient on Ma and selected geometric characteristics. The function was then used in external ballistics trajectory simulations to identify the geometry that maximizes impact velocity, which serves as the optimization criterion.

To obtain realistic and reliable results, the numerical twin must be an accurate counterpart of the physical projectile. Therefore, a significant part of this work is devoted to the assessment

*e-mail: krzysztof.piasta@wat.edu.pl

Manuscript submitted 2025-09-01, revised 2025-12-12, initially accepted for publication 2025-12-22, published in March 2026.

and validation of the numerical model. Estimating aerodynamic coefficients with CFD requires different modeling strategies depending on the coefficient of interest. Selecting an appropriate solver (steady-state or time-dependent), choosing a turbulence model, and ensuring adequate domain discretization are all critical decisions influenced by specific flow phenomena under consideration. In [4–11], the authors conducted flight simulations of 5.56 mm and 12.7 mm projectiles in steady-state and transient regimes, demonstrating that Reynolds-averaged Navier-Stokes (RANS) computations can accurately estimate static aerodynamic coefficients. However, dynamic derivatives, such as the Magnus effect in subsonic and transonic regimes or pitch-damping moment, often require transient large eddy simulations (LES) or hybrid RANS-LES approaches.

In the context of projectile shape optimization, while the influence of certain geometric features on drag was established by McCoy and Carlucci [2, 3], other aspects were examined in greater detail using CFD methods. For example, in [12], the author analyzed drag coefficients of four different 5.56 mm projectiles at various Ma using Ansys Fluent software. A two-dimensional model was first validated against the known drag coefficient of a sphere before assessing the effects of total length, boattail angle, ogive shape and length, and méplat size (the flat, circular surface at the tip of the projectile nose). In [13], the same software was used in combination with both the two-equation k-ω Shear Stress Transport (SST) and one-equation Spalart-Allmaras (S-A) turbulence models to estimate pressure and skin friction drag coefficients for a rotating 120 mm projectile over a wide velocity range. The results were compared with semi-empirical predictions from the PRODAS software. One geometric factor that necessitates three-dimensional CFD modeling is the analysis of rifling grooves engraved on the projectile surface. In [14], the authors explored drag minimization through shape modifications using 3D CFD simulations with the S-A turbulence model within a RANS solver. They examined spiral grooves extending along the body and straight grooves limited to the boattail, reporting up to a 12.4% reduction in drag coefficient for certain configurations. Another investigation [15] assessed the impact of rifling grooves on Magnus force and roll-damping moment, highlighting that grooves significantly influence these dynamic forces, while their effect on drag under zero-yaw conditions is minimal. For cases involving yaw and rotation, more computationally intensive time-dependent simulations were required.

Further optimization efforts focused on the projectile base. In [16, 17], the bullet base was studied extensively. In [18, 19], researchers demonstrated base drag reduction for a 155 mm artillery shell using axisymmetric RANS models and multiple turbulence models. These studies confirmed that an axisymmetric assumption can reliably estimate the static drag coefficient for non-yawing motion. In [20], a novel passive control strategy employing a porous surface on the boattail and base resulted in a 23% drag reduction and nearly eliminated the Magnus force. Additional work in [21, 22] evaluated porous surfaces in transonic flow, showing drag reductions of approximately 8% with axisymmetric RANS simulations using the Baldwin-Lomax turbulence model.

The shape and geometry of the projectile nose and ogive substantially affect the flow field, pressure distribution, and shock wave structure, collectively influencing drag [10, 11, 23]. For instance, in [24], a hybrid ogive profile combining a tangent ogive and a secant ogive was analyzed using steady-state axisymmetric CFD with the S-A turbulence model across subsonic, transonic, and supersonic regimes. In our earlier research [25, 26], the effect of méplat size on drag was investigated, and we identified an optimal ratio of méplat diameter to projectile diameter between 0.12 and 0.15. A two-dimensional k-ω SST model was employed for that analysis. We established an experimental method for estimating the drag coefficient of the 5.56 mm M193 projectile. This data was used to validate a 2D CFD model employing the same turbulence modeling approach. The 7.4% discrepancy between the CFD and experimental drag coefficients confirmed that the 2D model yielded sufficiently accurate results.

The literature reviewed above confirms that steady-state simulations are a suitable tool for estimating the drag coefficient. Moreover, since barrel rifling does not significantly influence drag under zero-yaw conditions, it can be omitted from the model, justifying the use of a two-dimensional axisymmetric assumption. While applying a porous surface on the boattail and base of a bullet is an interesting concept, it could be equally beneficial for an optimized shape. Therefore, this design feature is excluded from the methodology in the present study.

As stated before, investigating the individual effect of each geometric factor on drag can be time-consuming and potentially misleading due to overlooked parameter interactions. To address this, the DOE methodology was applied to develop a response surface describing the drag coefficient as a function of selected geometric variables. DOE proved valuable in defense-related research: in [27], the method was successfully applied in simulations to assess how various parameters affect the braking mechanism in a gas-delayed blowback operation firearm; in [28], the authors implemented a face-centered composite design plan in wind tunnel tests of a 155 mm projectile to analyze the response surface of Magnus and spin-damping coefficients. Their approach significantly reduced the cost and time associated with traditional one-factor-at-a-time testing methods. In another study [29], DOE coupled with a neural network and a genetic algorithm was used to maximize projectile range and impact velocity, while minimizing the angle of attack. A further application is shown in [30], where an optimization algorithm was used to enhance muzzle velocity by adjusting peak pressure, chamber volume, and propellant charge density of a cased-telescoped ammunition, resulting in a 14 m/s increase in muzzle velocity. In [31], genetic algorithms with results of PRODAS and CFD estimations were used for shape optimization of the 155 mm artillery projectile.

The algorithms confirmed theoretical data presented in [2, 3, 32] concerning the least-drag characteristics of boattail angle (at 7°), ogive radius (twice the tangent ogive radius), and méplat diameter (0.12 of the projectile diameter). The cited studies employing DOE methods focused primarily on interior ballistics or on the exterior ballistics of artillery projectiles. In exterior ballistics optimization research [31], system responses were determined mainly using the semi-empirical PRODAS software,

with CFD simulations serving as a comparative reference to highlight the tool-dependent variability of the results. In the present work, which investigates small-arms exterior ballistics, the use of a carefully designed DOE framework enabled the authors to develop a reliable numerical twin based on CFD models, demonstrating clear advantages over semi-empirical approaches.

Building on these developments, this work integrates CFD-based aerodynamic estimation and DOE methodology to establish a numerical twin of a small-arms projectile for its external shape optimization. The numerical model supports an in-depth examination of the effects of geometric parameters on aerodynamic drag and terminal velocity. The construction of the CFD model is explained, detailing solver selection, mesh sensitivity study, and the estimation of an aerodynamic coefficient for an exemplary small-arms projectile. The CFD model is then validated based on the available results of 5.56×45 mm projectile experimental drag estimations. A structured experimental plan is then implemented to develop an approximating function of the drag coefficient as a function of Ma and geometric variables for a perspective 7-mm-diameter projectile. This function is incorporated into a ballistic trajectory model to predict performance metrics and identify optimal configurations. The second experimental plan is then conducted to approximate the terminal velocity for a perspective projectile for exemplary initial conditions, and the resulting objective function is employed in an optimization tool. This integrated approach contributes to a more comprehensive understanding of geometric influences and supports the design of higher-performance projectile configurations.

2. METHODS

2.1. Governing equations

The governing equations in CFD simulations are the continuity and momentum equations of fluid mechanics. Given the high Reynolds numbers associated with supersonic projectile flight, the flow exhibits turbulent fluctuations across multiple scales. To resolve this, the Reynolds-averaged Navier-Stokes (RANS) equations are employed.

Following the assumption of 2D axisymmetric flow (zero-yaw angle), the governing equations for the mean flow field can be expressed as follows [33, 34]:

$$\frac{\partial \rho}{\partial t}+\frac{\partial}{\partial x_i}\left(\rho \bar{u}_i\right)=0, \tag{1}$$

$$\begin{aligned}\frac{\partial}{\partial t}\left(\rho \bar{u}_i\right)+\frac{\partial}{\partial x_j}\left(\rho \bar{u}_i \bar{u}_j\right) &= -\frac{\partial \bar{p}}{\partial x_i}+\frac{\partial}{\partial x_j}\left[\mu\left(\frac{\partial \bar{u}_i}{\partial x_j}+\frac{\partial \bar{u}_j}{\partial x_i}-\frac{2}{3}\delta_{ij}\frac{\partial \bar{u}_l}{\partial x_l}\right)\right] \\ &\quad +\frac{\partial}{\partial x_j}\left(-\rho\overline{u_i' u_j'}\right),\end{aligned} \tag{2}$$

where ρ is the density of the medium, $\bar{u}$ is the time-averaged velocity component, $\bar{p}$ is the mean static pressure, μ is the molecular viscosity, and δ is the Kronecker delta.

The term $-\rho\overline{u_i' u_j'}$ in (2) represents the effects of turbulence and is called Reynolds stresses. It accounts for the momentum transport due to velocity fluctuations. To close (2) Reynolds stresses must be modeled, and for this purpose, various turbulence models may be employed. The effects of employing various turbulence models on the flow variables and computational model convergence are analyzed in the model validation in Section 2.3.

2.2. Computational model

The numerical twin for the simulations was established in Ansys Fluent 2022R2 software, with part of the postprocessing performed in version 2024R1. To validate the developed two-dimensional CFD model, the process relied on existing experimental data for a real-world projectile. Specifically, the 5.56×45 mm M855 cartridge projectile was selected as the reference since experimental drag measurements are available in the literature. Due to the assumption of axisymmetry in the two-dimensional model, the real-world scenario is simplified to a case of a zero-yawing motion of a projectile in flight. As stated before, in the case of a relatively high Ma (short distance to target), this assumption yields acceptable results. A model validated for this reference projectile is assumed to provide sufficiently accurate predictions for similar prospective projectiles with comparable shapes and aerodynamic characteristics.

The nominal geometry of the projectile used in the 5.56×45 mm M855 cartridge was employed as a reference for modeling, based on [35]. For simulation (generating an excellent quality 2D mesh around the projectile geometry), the geometry was simplified by omitting the rounded base profile and replacing it with a sharp corner, as well as removing the cannelure on the cylindrical section of the projectile. The model was set up for Mach 2.68, corresponding to the velocity for which experimental data are available. An unstructured, two-dimensional mesh with axisymmetric boundary was generated using the Ansys Meshing tool. To establish a sufficiently large computational domain and ensure resolved wake flow, based on the best practices and previous analyses [26, 36, 37], the domain was stretched approximately 18 projectile diameters radially, 14 diameters towards the inflow, and 30 diameters rearwards to the outflow, so that the far-field boundary condition exhibited non-disturbed flow variables. Pressure far-field boundary conditions were employed with the operating pressure of 101 325 Pa and both far-field and outlet boundaries with 1% turbulence intensity and turbulent viscosity ratio set to 2. The nondimensional wall distance (y^+), which is a critical parameter for accurately resolving the boundary layer, was maintained below 1.0 across the entire surface of the projectile. This requirement resulted in an initial mesh comprising over one million cells. The computational domain and mesh characteristics are presented in Fig. 1 and Table 1 below.

Both density-based and pressure-based solvers employing implicit formulations were used in combination with three different turbulence models to identify the most suitable computational approach: one-equation Spalart-Almaras, two-equation Realizable k-ε and two-equation k-ω Shear Stress Transport. Air density was treated as a variable governed by the ideal gas law,

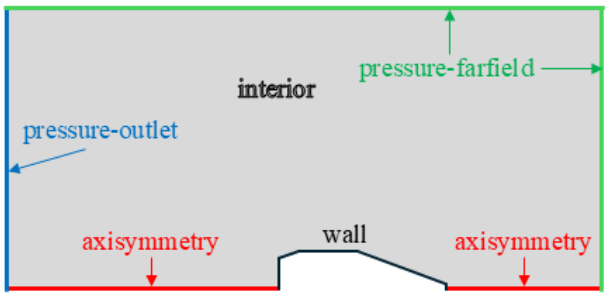

Fig. 1. Schematic of the domain boundaries for solver setup

Table 1
Discretization parameters and metrics of the initial mesh

Parameter	Value
Number of elements (–)	1 076 400
Required max. first cell height (μm)	0.80
Max. y^+ (–)	0.5
Max. skewness (–)	0.20
Avg. skewness (–)	0.03
Max. aspect ratio (–)	1782
Avg. aspect ratio (–)	85
Min. orthogonal quality (–)	0.95
Avg. orthogonal quality (–)	0.99

while viscosity was computed according to Sutherland's law. Initial simulations were conducted with the first-order upwind discretization scheme coupled with Roe-FDS flux splitting and a Courant number of 0.8. Following convergence of the initial solution, the discretization was refined to a second-order upwind scheme for improved accuracy.

The simulations were performed in parallel on 16 cores of the Intel Core i9-13900F processor with 32 GB DDR5 5200 MHz of RAM. No convergence acceleration methods were used to avoid any influence of those methods on the final solution. The following convergence criteria were employed: all the flow residuals to be reduced at least four orders of magnitude, with the drag coefficient variation limited to less than 0.001 over a span of 1000 iterations. Ultimately, the variation in drag coefficient served as the principal criterion for evaluating convergence in all cases. The average time for each simulation was about 3 hours in cases with achieved convergence.

2.3. Model validation

The model was validated both qualitatively, by examining the flow fields, and quantitatively, by comparing the estimated zero-yaw drag coefficient with experimental data.

2.3.1. Turbulence model

The initial step involved evaluating each solver setup under different turbulence models. The analysis of density and velocity fields, along with velocity vectors at the surface vicinity, was conducted, as illustrated in Figs. 2–5. It is important to note that only the density-based (d-b) solvers provided convergence, while the pressure-based (p-b) solvers failed to successfully establish a stable value of the analyzed variable – the drag coefficient value was oscillating.

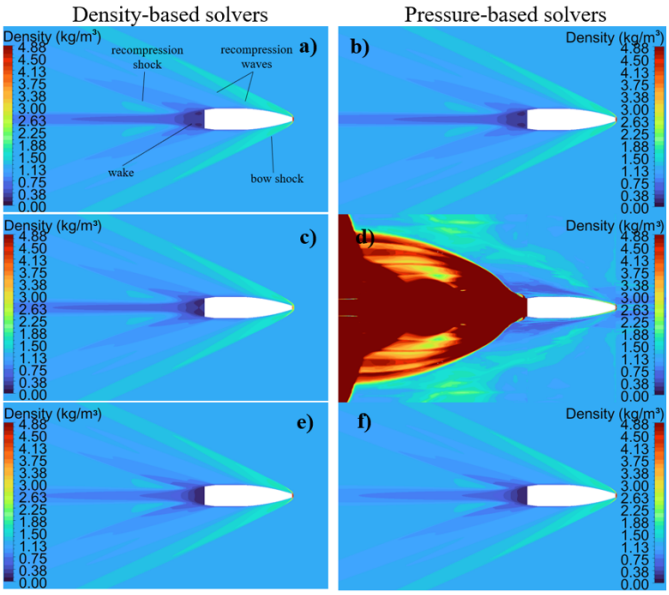

Fig. 2. Density fields obtained with CFD simulations – M855 projectile at Mach 2.68: (a) d-b k-ω SST, (b) p-b k-ω SST, (c) d-b k-ε Realizable, (d) p-b k-ε Realizable, (e) d-b S-A, (f) p-b S-A

The density fields obtained from the simulations provide insights into the flow behavior around the surface of the projectile. Upon initial inspection, the pressure-based solver with the k-ε realizable turbulence model failed to simulate a stable flow field, as expected due to the solver divergence (Fig. 2d). Consequently, this solver configuration is deemed unsuitable for the analyzed application and will not be considered in future analyses. Each of the remaining solutions exhibits a reasonable representation of the flow, characterized by supersonic velocities across the entire surface of the projectile, except for the base region and a small local subsonic area near the blunt nose. This flow pattern aligns with the literature [10, 38, 39]. All notable features of the flow field are illustrated in Fig. 2a. The bow shock is visible close to the projectile nose with a small standoff and can be considered oblique due to the high flow freestream velocity. Additionally, expansion waves are evident at the junctions of the ogive-cylinder and cylinder-boattail. The recompression shock is observed immediately aft of the projectile base and propagates at a steep angle toward the outlet. Downstream the projectile, a wake region is visible, characterized by extremely low velocity magnitude and pressure extending up to approximately two projectile diameters.

The criteria for selecting the turbulence model appropriate for the investigated phenomenon were based on an analysis of velocity and density fields, as well as the distribution of flow vectors in characteristic regions of the flow: the base region, the projectile méplat area, and the near-wall boundary layer.

A discrepancy arises in the low-velocity region at the projectile tip, where the bow shock forms when comparing the k-ω SST and k-ε Realizable turbulence models. To examine this local flow field more closely, the velocity distributions around the méplat are provided in Fig. 3 below.

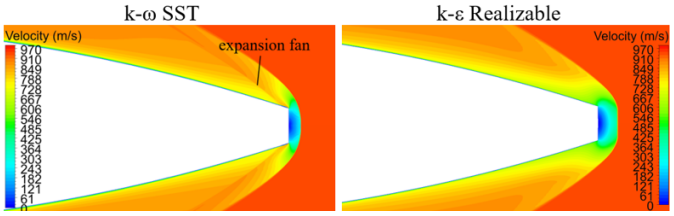

Fig. 3. Velocity fields in the vicinity of the projectile méplat: left – k-ω SST, right – k-ε Realizable turbulence model

Analyzing the flow field in Fig. 3, the flow velocity at the wedge increases through an expansion fan following the Prandtl-Meyer theory. The local subsonic region appears in the vicinity of the vertical surface of the méplat, transitioning to supersonic as it follows the shockwave contour [40]. In contrast, the k-ε Realizable density-based model fails to recognize the expansion fan at the edge of the méplat. The méplat region itself is inaccurately predicted, exhibiting a greater stand-off to a vertical part of the shockwave, which should not occur at the analyzed velocity.

To further evaluate the ability of the k-ω SST solver to resolve the flow, the boundary layer was analyzed by depicting the velocity vectors in the vicinity of the surface of the projectile (Fig. 4).

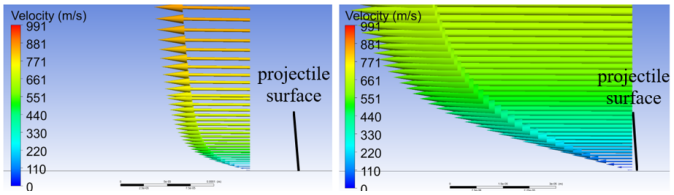

Fig. 4. Velocity vectors obtained with the k-ω SST turbulence model: left – far from the boundary, right – close to the surface

The velocity vectors in Fig. 4 are extracted from the computational domain along a control line perpendicular to the main flow direction, located at the middle of the cylindrical part of the bullet geometry. The boundary layer region is accurately resolved, in agreement with findings reported in the literature [41]. The velocity at the wall (at the projectile surface) is zero, due to the no-slip condition, gradually increasing within the boundary layer until it reaches approximately 90% of the free-stream velocity. Consequently, the model addresses the boundary layer problem adequately.

Examining the base region obtained with each turbulence model, a visible difference emerges between the k-ω SST and S-A models regarding the extent of the low-density, low-velocity region (Fig. 2a, 2e). The former produces a more elongated region, extending behind the projectile and generating a trailing shock, whereas the latter yields a comparatively shorter and more confined region of one diameter. A spark shadowgraph image at Mach 2.61, presented by Silton [35], suggests that the base region predicted by the k-ω SST model aligns more closely with experimental observations. Figure 5 illustrates the velocity field and the velocity vectors in the base region for the density-based solver with the k-ω SST turbulence model.

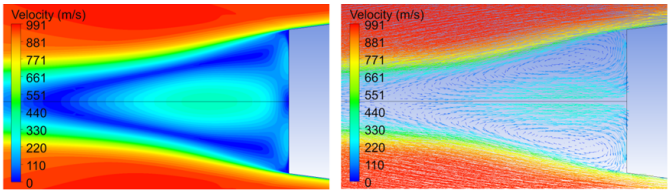

Fig. 5. Base region obtained with the k-ω SST turbulence model: left – velocity field, right – velocity vectors

In this local subsonic base region, the velocity vectors exhibit low magnitudes, and flow separation generates vortices just aft of the projectile base corner. These features agree with the literature, indicating that the k-ω SST turbulence model accurately resolves the flow [17–19, 42].

Consequently, based on these findings, the density-based k-ω SST turbulence model was deemed most suitable for the present analysis.

2.3.2. Drag coefficient estimation

To evaluate the sensitivity of the CFD simulations to domain discretization, a mesh refinement study was conducted. Starting from the initial mesh (Mesh No. 4), three coarser and two finer meshes were generated, ensuring that the y^+ value remained below 1.0 along the entire projectile surface. Simulations were subsequently performed on each mesh utilizing identical solver settings and following the same calculation procedure. Mesh metrics and resulting drag estimates are summarized in Table 2 and Fig. 6.

The mesh refinement study indicates that, for the specified domain size, geometry, and solver settings, a mesh with at least 870 000 elements is required to ensure solver convergence and

Table 2
Mesh refinement study results

Parameter	Mesh number					
	1	2	3	4	5	6
Number of elements ($\times 10^3$)	684	755	872	1080	1330	1550
First cell height (μm)	0.41	0.40	0.38	0.38	0.36	0.32
Max. skewness (–)	0.20	0.20	0.20	0.20	0.20	0.20
Min. orthogonal quality (–)	0.95	0.95	0.95	0.95	0.95	0.95
Max. aspect ratio (–)	2299	2173	1785	1782	1599	1530
Drag coefficient (–)	–	–	0.2610	0.2609	0.2608	0.2608

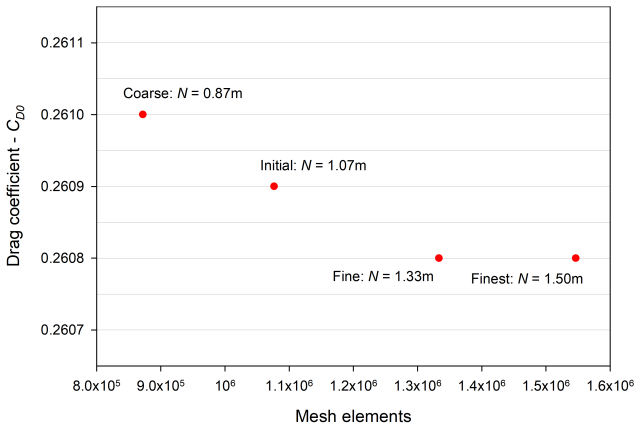

Fig. 6. Estimated drag coefficient dependence on the number of mesh elements

a stable solution. Coarser meshes (No. 1 and 2) failed to provide solver convergence. To verify the mesh convergence, the drag coefficient obtained with the finest mesh (Mesh No. 6) was compared with the value from the initial mesh (Mesh No. 4):

$$e = \left| \frac{C_{D6} - C_{D4}}{C_{D4}} \right| = 0.04\%. \tag{3}$$

The value of e characterizes the convergence of the method. It indicates that the difference in the estimated drag coefficient between the initial and finest meshes in the analyzed case is negligibly small. The solutions obtained using meshes with 0.87 million and 1.33 million elements remain invariant as the mesh is further refined, while the required computational time increases significantly. Therefore, the mesh containing approximately 0.87 million cells is considered sufficient for the analyzed supersonic flow over an axisymmetric projectile and will be used in subsequent simulations.

Figure 7 presents a comparative analysis of the drag coefficient for the M855 projectile, including simulation results, experimental data from the literature [43], and semi-empirical estimates conducted by the authors using Arrow Tech PRODAS software [44].

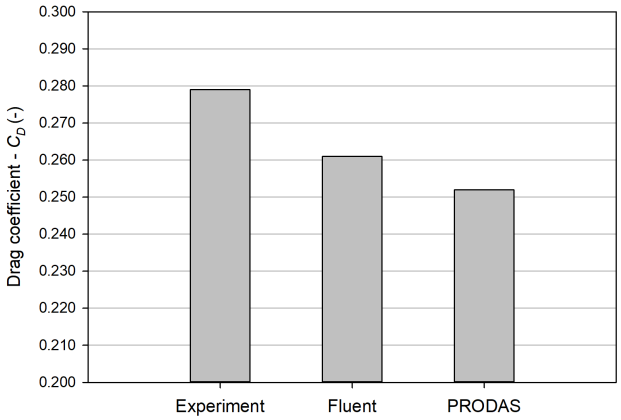

Fig. 7. Comparison of the M855 projectile drag coefficient estimations at Mach 2.68 with experimental and semi-empirical results

The drag coefficient of the 5.56 mm M855 projectile derived from numerical experiments ($C_{D0} = 0.261$) is 6.45% lower than the experimental value reported by the authors ($C_D = 0.279$, after excluding one measurement that exceeded two standard deviations from the mean) [43]. This discrepancy is primarily attributed to geometric differences between the actual projectile used in the experiment and the nominal geometry simplified for the CFD model, as well as the assumption of axisymmetry in the numerical twin. Nevertheless, when compared to the semi-empirical estimate ($C_{D0} = 0.252$), which shows a discrepancy of over 9.68%, the CFD result is considered satisfactory.

After validating the CFD model on the 5.56 mm M855 projectile, the same modeling approach can be applied to a prospective projectile design with different dimensions. The use of a validated numerical twin for a similar supersonic projectile shape ensures the reliability of the aerodynamic estimations across both configurations.

2.4. Experimental plan

An exemplary experimental plan was developed for a prospective 7 mm-diameter boat-tail secant-ogive projectile. The zero-yaw drag coefficient, as the response function of interest, depends on several factors and can be represented as:

$$C_{D0} = F\left(Ma, D, D_M, D_B, L, l_B, l_C, l_O, \alpha_B, R_O\right), \tag{4}$$

where D, D_B, D_M are the diameters of projectile geometry parts: projectile, base, and méplat; L is the projectile overall length; l_B, l_C, l_O are projectile geometry part lengths: boattail, cylindrical; ogive, α_B is the boattail angle and R_O is the ogive radius.

The external shape of the projectile is simplified, with sharp corners of the base and méplat, as well as by the lack of cannelure on the cylindrical part of the geometry.

2.4.1. Factors definition

To implement the experimental plan, each factor was thoroughly examined to determine which variables should remain constant and to define appropriate ranges of variation for the others. Chosen ranges can be modified, as the proposed methodology applies to any configuration of constants and variables.

Starting with the **Mach number**: in CFD simulations, the only variable in the Ma equation is the projectile velocity. Therefore, in this analysis, Ma is considered a function of velocity. Given the expected high terminal kinetic energy and a target distance of no more than 300 meters, initial and terminal velocities were estimated to range from 700 m/s, which is the lowest velocity that would provide the required terminal ballistics, to 950 m/s, which is the highest muzzle velocity for the lightest projectile, for the projectile weight ranging from 6.0 to 8.8 g. Including a safety margin, the Ma range for the experimental plan was established between Mach 2.0 and Mach 2.75.

The **diameter** of the proposed **projectile** was defined in previously published preliminary research [45]. Without delving into further details – given the illustrative nature of this experimental plan – a constant diameter of 7.0 mm was chosen for the following analysis.

The factor range for overall **projectile length** was assessed based on available literature and existing projectile designs, while considering a weight requirement (maximum 8.8 g) and using CAD-based mass estimations. For a 7 mm diameter projectile, the overall length was set to vary between 30 mm and 36 mm.

Projectile length is directly related to three subcomponents: boattail length, cylindrical length, and ogive length. As shown in the literature review in Section 1, the cylindrical part has the least direct impact on drag reduction. However, increasing the boattail and ogive lengths for better aerodynamic performance should not excessively reduce the cylindrical length, as it provides the bearing surface for barrel engagement – critical for accuracy and precision. This relationship is described by the following equation:

$$l_C = L - l_B - l_O \,. \tag{5}$$

The analysis of existing modern bullets and literature shows that a minimum length of a bearing surface (**cylindrical part**) of at least 1.10÷1.25 projectile diameter is required to ensure stable alignment with rifling. Thus, in this study, the minimum cylindrical length is set to 8 mm.

The **boattail length** effect on the drag coefficient is straightforward – longer boattail results in a lower drag coefficient for supersonic flight; however, it can negatively impact dynamic stability and thus decrease accuracy and precision. According to McCoy [2], practical boattail lengths range from 0.5 to 1.0 times the projectile diameter. Accordingly, boattail length in this study will vary between 3.5 mm and 7.0 mm.

Considering the **ogive length**, longer ogives provide a lower drag coefficient for both low and high supersonic speeds. Although there is no specific ratio of ogive length to projectile diameter that is universally practical, the length should be maximized within the constraints of the other lengths – boattail and cylindrical parts. To maintain a reasonable ratio between the ogive length and projectile diameter, the minimal value of the ogive length in the plan was set to 16 mm.

Another variable characterizing the ogive geometry is its **radius**. The results of preliminary analysis of the sensitivity of tangent and secant ogive profiled projectiles to seating depth [46] indicate that secant profile projectiles are slightly more sensitive to seating depth; however, the differences were minimal and could be affected by other factors such as variations in internal and external dimensions, inconsistent propellant powder filling, and variations in ogive shape and méplat diameter. Therefore, a secant ogive profile was chosen for the analysis, with the R_T/R_O ratio of 0.5, with the profile radius two times longer than a tangent profile for the same ogive length, optimal according to McCoy and Carlucci, as confirmed in the recent literature, e.g., by Zeidler in [31]. Hence, the ogive radius in the analysis is a function of one variable – ogive length.

The **boattail angle** directly affects the base and wave drag components of the overall drag, significantly altering the drag coefficient. A higher value of the boattail angle results in a greater reduction of the low-pressure base region after the bullet, reducing the base pressure component of the drag. However, when the angle is too steep, the flow begins to separate at the boattail angle, first creating shockwaves, and eventually, at extremely steep angles, it separates leading to a drastic increase in the low-pressure region. Preliminary CFD and semi-empirical simulations confirmed the literature data [2,3,31], indicating the lowest drag at supersonic speeds at 7° of boattail angle, which was set as a constant in the plan.

The **base diameter** of the projectile is determined by the boattail angle and length. Given the fixed boattail angle of 7°, the base diameter becomes a function of the boattail length alone.

The **méplat diameter**, strongly dependent on the projectile design and manufacturing technology, significantly affects the drag coefficient. Prior analysis [25] demonstrated that for a small arms projectile, the lowest average drag for supersonic flow was achieved with a méplat diameter to projectile diameter ratio of 0.12. This value is coherent with the literature [2, 3, 31]. Therefore, for a 7.0 mm diameter projectile, the méplat diameter was set constant at 0.84 mm.

With the minimum bearing surface and boattail lengths defined, the maximum possible ogive length can be calculated as follows:

$$l_{O\,\max} = L_{\max} - l_{C\,\min} - l_{B\,\min} = 36.0 - 8.0 - 3.5 = 24.5 \text{ mm}.$$

Conversely, using the minimum ogive length, the maximum cylindrical length is:

$$l_{C\,\max} = L_{\max} - l_{B\,\min} - l_{O\,\min} = 36.0 - 3.5 - 16.0 = 16.5 \text{ mm}.$$

Based on the parameter analysis, the factors used in the approximation function are listed in Table 3.

Table 3
Drag coefficient function parameters

Variable	Unit	
Ma	–	2.00÷2.75
D	mm	7.0
D_M	mm	0.84
D_B	mm	$g(l_B)$
L	mm	30÷36
l_B	mm	3.5÷7.0
l_C	mm	8.0÷16.5
l_O	mm	16.0÷24.5
α_B	deg.	7.0
R_O	mm	$h(l_O)$

Following the data presented in Table 3, it can be concluded that – after reducing the number of variables – the Ma and the lengths of the projectile and its individual sections remain the only variable factors influencing the objective function. Since the cylindrical section length is defined by the values of the other three length parameters, the following variables were selected for the experimental plan:

- $x1$: Ma (ranging from 2 to 2.75)
- $x2$: projectile overall length (ranging from 30 mm to 36 mm)
- $x3$: projectile boattail length (ranging from 3.5 mm to 7.0 mm)
- $x4$: projectile ogive length (ranging from 16.0 mm to 24.5 mm)

To visualize the specified factors, the projectile geometry, including all the characteristics analyzed above, is presented in Fig. 8 below.

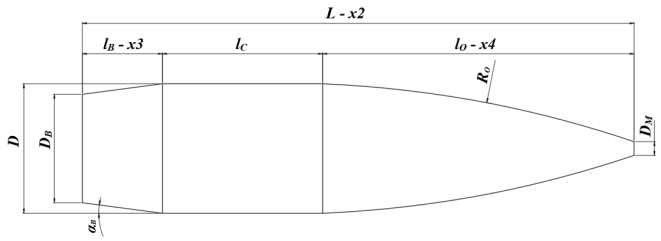

Fig. 8. Analyzed projectile geometry with chosen factors

The minimal length of the cylindrical part – l_c is not enforced during the optimization process, to avoid restricting the function. However, it will be employed in the tool designed further on in MATLAB, and the user will be informed if the restriction of the minimum l_c value is not met.

2.4.2. Execution of the plan

For studies involving three to seven factors, Hartley or Bi-experimental designs are often preferable due to their efficiency and the small number of experimental runs required. In the present case, a composite Hartley design with four factors was employed. The relation between coded and uncoded values of the chosen parameters in DOE is given by the following formula [47, 48]:

$$X_k = \alpha \frac{x_k - (x_{k\max} + x_{k\min})}{x_{k\max} - x_{k\min}}, \tag{6}$$

where X_k is the coded value of the k-th factor, α is the star arm, $x_{k\max}$ is the maximum, and $x_{k\min}$ is the minimum value of the k-th uncoded factor.

The plan matrix, including both coded and uncoded factor values, as well as the results of the CFD-based drag coefficient estimations, is presented in Table 4. The CFD results of C_{D0} estimations were achieved by implementing each treatment – projectile geometry and Ma – to the validated two-dimensional model explained in the earlier section.

The Hartley plan is a composite design consisting of three components: a core set (first 8 runs), axial, or star points (runs 9–16, star arm $\alpha = 2$, and a central point (run 17). Simulations were performed for all 17 treatments, requiring a total of approximately 34 hours of computational time (about 2 hours per simulation). Given the nature of computer experiments, where random experimental error is absent, and only the discretization difference must be considered, a full statistical analysis for each treatment is omitted [49].

Table 4
Hartley plan PS/DS-P:Ha4 and results of numerical experiments for C_{D0}

Plan									C_{D0}
	Coded factors				Uncoded factors				
n	X_1	X_2	X_3	X_4	$x1$	$x2$	$x3$	$x4$	z
1	–1	–1	–1	–1	2.188	31.5	4.375	18.125	0.2520
2	1	–1	–1	1	2.563	31.5	4.375	22.375	0.2049
3	–1	1	–1	1	2.188	34.5	4.375	22.375	0.2304
4	1	1	–1	–1	2.563	34.5	4.375	18.125	0.2266
5	–1	–1	1	1	2.188	31.5	6.125	22.375	0.2243
6	1	–1	1	–1	2.563	31.5	6.125	18.125	0.2315
7	–1	1	1	–1	2.188	34.5	6.125	18.125	0.2459
8	1	1	1	1	2.563	34.5	6.125	22.375	0.1999
9	–2	0	0	0	2.000	33.0	5.250	20.250	0.2509
10	2	0	0	0	2.750	33.0	5.250	20.250	0.2010
11	0	–2	0	0	2.375	30.0	5.250	20.250	0.2233
12	0	2	0	0	2.375	36.0	5.250	20.250	0.2240
13	0	0	–2	0	2.375	33.0	3.500	20.250	0.2297
14	0	0	2	0	2.375	33.0	7.000	20.250	0.2176
15	0	0	0	–2	2.375	33.0	5.250	16.000	0.2532
16	0	0	0	2	2.375	33.0	5.250	24.500	0.2071
17	0	0	0	0	2.375	33.0	5.250	20.250	0.2233

3. RESULTS AND DISCUSSION

3.1. Objective function

The object response, i.e., zero-yaw drag coefficient derived from the plan, can be approximated by a quadratic function:

$$C_{D0} = \begin{pmatrix} 223.3 - 11.85X_1 - 0.53X_2 - 2.28X_3 \\ -11.79X_4 + 0.79X_1^2 + 0.22X_2^2 \\ +0.22X_3^2 + 1.85X_4^2 \end{pmatrix} \cdot 10^{-3}. \tag{7}$$

The objective function is a second-order response surface model equation. It includes both linear and quadratic terms, while the interaction terms were excluded to prevent overfitting (noticed during the analyses). The idea behind this methodology is to identify the stationary point of the response surface of the object, which in this case is the point of minimum response – the lowest value of the drag coefficient [50]. The analysis of the magnitude of the coefficients associated with each factor reveals that X_1 (Ma) and X_4 (bullet ogive length) have the greatest impact on the value of the response, while X_2 (overall length) and X_3 (boattail length) are less significant. Although the pronounced effect of the Ma on the drag coefficient aligns with expectations, the observation that the ogive length has a stronger influence than overall length provides useful guidance for the aerodynamic optimization of future projectile designs.

The adequacy of the approximation function was evaluated using the multiple correlation coefficient R. The correlation coefficient is used to evaluate how well a given model fits the observed data. It includes values between 0 and 1, where 0 indicates no correlation and 1 indicates perfect correlation. In the context of experimental data fitting, an R value greater than 0.95 is considered acceptable. However, for numerical experiments, a higher threshold is applied – typically higher than 0.99 – to confidently assume that the model accurately represents the underlying physical behavior. The multiple correlation coefficient is computed as:

$$R = \sqrt{\frac{\text{SSM}}{\text{SST}}} = \sqrt{\frac{\sum (\hat{y} - \bar{y})^2}{\sum (y - \bar{y})^2}} = 0.992, \tag{8}$$

where SSM represents the sum of squares for the model, SST is the total sum of squares, y is the experimentally estimated value of the response for each treatment, $\bar{y}$ represents the average value of the response, and $\hat{y}$ is the approximated value of the response.

Accordingly, the model explains over 99.2% of the variability in the response. To assess this adequacy, the coefficient of determination R^2 was estimated at 0.984. The values of R and R^2 indicate that the model can be considered adequate [48, 51]. To illustrate the accuracy of the drag coefficient approximation across different factor settings, three randomly selected sample treatments are presented in Table 5.

Table 5
Exemplary results of objective function approximation

Parameter	Value		
Ma $x1$	2.1875	2.5625	2.0000
Projectile overall length $x2$	34.5	34.5	33.0
Boattail length $x3$	6.125	6.125	5.250
Ogive length $x4$	18.125	22.375	20.250
C_{D0}	0.2459	0.1999	0.2509
C_{D0} approx.	0.2472	0.1999	0.2502
Square error	0.0000017623	0.0000000001	0.0000005384

A visualization of the correlation between the approximating function and the experimentally derived drag coefficient values, where the squared error is on the order of 10^{-6} or lower, confirms that the quadratic function without interaction terms provides sufficient accuracy for further analysis.

3.2. Trajectory modeling

The approximation function described in (7) was integrated into a validated in-house modified point-mass trajectory (PMT) solver in MATLAB R2023B software. In standard PMT modeling, the projectile is considered a point in space, with given mass and average coefficient of drag. Due to the short distances to the target analyzed (max. 300 meters) and small elevation angles, the PMT model is deemed sufficient [2, 3]. In the study presented, the projectile equations of motion incorporate a drag coefficient value that is recalculated at each timestep using the DOE-derived function shown in equation (7). For the cases where the projectile velocity during simulated flight exceeds or drops below the objective function range, with muzzle velocity higher than Mach 2.75, or with distance to the target causing velocity to drop below Mach 2, the program extrapolates the drag coefficient value. However, it is important to note that the adopted DOE framework constrains the accuracy of the method to the predefined factor ranges. The extrapolation presented here is performed solely for comparative purposes, to demonstrate the behavior of the tool beyond the Ma range used in the DOE. Table 6 contains outcomes from a series of simulations under various, randomly chosen initial conditions. Note that for some cases, the parameters were intentionally selected to exceed the established factor ranges. Consequently, the resulting predictions may exhibit discrepancies arising from extrapolation. The generated PMT solver employs the data as input and calculates trajectories with a variable drag coefficient for any given fire input data describing the desired projectile.

Comparison of the results for a chosen geometry with PRODAS software using a 4DOF trajectory modeling was conducted. The model employed in PRODAS was an FMJ steel/lead core, brass jacket projectile, with external geometry and overall pro-

Table 6
Exemplary results of trajectory analysis

Inputs	Simulation number				
	1	2	3	4	5
Projectile diameter (mm)	7.0	7.0	7.0	7.0	7.0
Projectile mass (g)	8.0	7.0	6.0	8.5	9.0
Overall length (mm)	35.0	33.0	32.0	36.0	30.0
Boattail length (mm)	4.5	6.0	5.0	7.0	3.5
Ogive length (mm)	18.0	20.0	19.0	20.0	16.0
Cylindrical length (mm)	12.5	7.0	8.0	9.0	10.5
Launch angle (deg.)	0.21	0.20	0.1	0.25	0.2
Crosswind speed (m/s)	2.0	3.0	2.0	3.0	4.0
Muzzle velocity (m/s)	900	920	950	850	900
Distance to the target (m)	300	300	500	200	100
Results	CFD-DOE PMT model				
Terminal velocity (m/s)	727.62	735.70	588.32	750.79	842.53
Terminal kinetic energy (J)	2117.8	1894.4	1038.4	2395.7	3194.4
Total deflection (m)	0.07	0.11	0.28	0.05	0.01
Time of flight (s)	0.37	0.36	0.67	0.25	0.11

jectile mass according to the data in Table 6 for each treatment. Naturally, the CFD-DOE PMT solver does not consider mass distribution in the bullet.

The trajectories calculated with both methods for the selected case of a 7.6 g projectile are shown in Fig. 9 and specific results can be analyzed in Table 7. The input data was chosen based on previous analysis and existing data for a given PRODAS model.

Table 7
CFD-DOE PMT and PRODAS trajectory results comparison

Inputs	Value			
Projectile diameter (mm)	7.0			
Projectile mass (g)	7.6			
Overall length (mm)	31.500			
Boattail length (mm)	4.375			
Ogive length (mm)	18.125			
Cylindrical length (mm)	9.000			
Launch angle (deg.)	0.23			
Crosswind speed (m/s)	0			
Muzzle velocity (m/s)	850			
Results	CFD-DOE PMT	PRODAS	Difference	Difference (%)
Maximum horizontal coordinate (m)	0.50	0.50	0.00	0
Max. horizontal coordinate range (m)	240.32	243.00	2.68	1.10
Velocity at 100 meters (m/s)	789.20	791.63	2.43	0.31
Velocity at 200 meters (m/s)	729.80	734.84	5.04	0.69
Velocity at 300 meters (m/s)	672.12	679.54	7.42	1.09
Terminal velocity (m/s)	588.91	596.34	7.43	1.25
Range (m)	452.27	456.66	4.39	0.96
Time of flight (s)	0.6385	0.6406	0.0020	0.33

The trajectories achieved with both 4DOF PRODAS and CFD-DOE PMT models align exceptionally well with each other for almost the whole flight. The highest discrepancies occur at the aft section of the projectile, where the projectile modeled with PRODAS is characterized by slightly higher velocity. The resulting range for chosen initial conditions is slightly higher than the one estimated with the CFD-DOE PMT method.

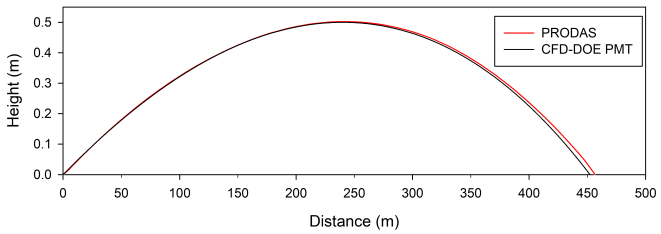

Fig. 9. Trajectory comparison of the projectile with exemplary inputs

Analysis of the values presented in Table 7 shows a remarkably high correlation between PRODAS estimations and the CFD-DOE PMT model. The former tends to predict slightly slower velocity reduction, resulting in higher (by max. 7.43 m/s – 1.25%) terminal velocity. The maximum horizontal coordinate is equal (±0.01 m), with a difference of the range at which the vortex appears of 2.68 ± 0.02 m.

The discrepancies between the two estimates arise from different drag coefficient estimation. A comparison of both drag curves for the velocities in question is shown in Fig. 10.

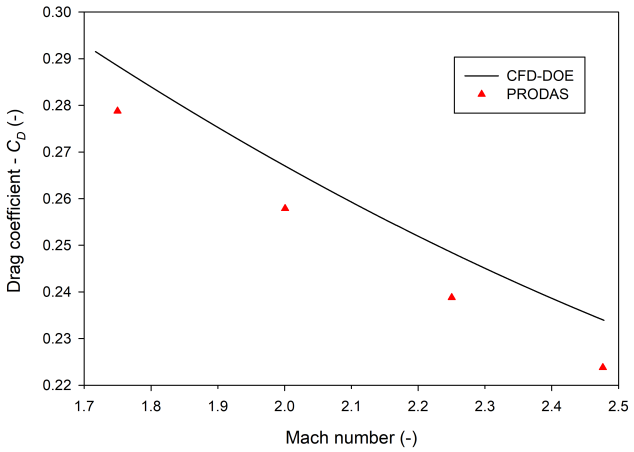

Fig. 10. Calculated drag coefficient of the exemplary projectile with an experimental plan and PRODAS software

Figure 10 indicates that PRODAS tends to underestimate the drag coefficient in the whole range of experienced Ma, as previously reported by the authors in [26] and mentioned in the literature [52], where semi-empirical drag estimates for a 155 mm projectile were lower than those from 2D CFD. In [13], researchers likewise observed lower C_D values predicted by PRODAS when compared to 3D CFD for a 120 mm projectile. As concluded by the authors, PRODAS is effective for quickly estimating aerodynamic coefficients for geometries similar to existing data. However, its predictive accuracy cannot be ensured when the geometry and flow conditions fall outside the database. In [31], the authors compared the drag coefficients estimated by PRODAS against CFD simulations for two 155 mm artillery projectiles. Their findings similarly show that PRODAS underestimated the coefficient in the whole Mach range. The discrepancies were dependent on similar geometries of the projectile in the program database, evidently affecting the results.

The quadratic objective function, which approximates the drag coefficient with a multiple correlation coefficient value of over 0.99, implemented in a point-mass trajectory model, results in range and terminal velocity predictions differing by 0.96% and 1.25%, respectively, from those generated by PRODAS. These discrepancies stem primarily from PRODAS underestimating the drag coefficient, as shown in Fig. 10. In practical terms, an underestimation of drag by 9.5% when using PRODAS can lead to an overestimation of effective range and terminal velocity. Considering these findings, the presented CFD-DOE PMT methodology offers more reliable estimates.

3.3. Shape optimization

The established methodology is applied to optimize the external shape of the projectile with respect to the achievable terminal velocity. Terminal velocity was selected as the optimization objective since it directly correlates with impact energy and effective range, which are considered key performance metrics for small arms projectiles. To develop an optimization tool capable of determining specific geometric parameters – while keeping selected features constant – a second experimental plan will be implemented. In this plan, the response variable is the terminal velocity of the projectile at the target, approximated as a function of selected shape-defining variables. This approximation is based on the combined CFD-DOE PMT model.

The optimization process focuses exclusively on the external shape of the projectile and does not consider modifications to its internal configuration. It is assumed that any change in external geometry can be compensated by adjusting the internal dimensions of the projectile components – such as jacket thickness or core density – to maintain a consistent mass and mass distribution. This approach isolates the aerodynamic effects of shape on drag coefficient and terminal kinetic energy, which are the primary objectives of the analysis. Consequently, the simulations did not include potential variations in muzzle velocity arising from unadjusted mass changes. In practical applications, any necessary adjustments to preserve projectile mass and interior ballistics performance would be addressed during detailed engineering design.

Regarding projectile stability, the optimization process was conducted for a velocity range corresponding to Mach 2–2.75, which are fully supersonic flight conditions. A zero-yaw motion assumption (2D axisymmetry) was adopted in the numerical twin construction, based on the expectation of negligibly small yaw angles within the range where the projectile remains above Mach 2 [2, 3]. Under these conditions, a projectile that exhibits adequate stability at the muzzle is expected to remain stable throughout the considered trajectory segment. Therefore, a gyroscopic stability factor of at least 1.5 was assumed to ensure sufficient spin stabilization and minimize the risk of dynamic instability.

3.3.1. Terminal velocity objective function

The projectile velocity at target V_T, within the PMT external ballistics model employed in these simulations, depends on multiple factors. It can be described by the following function:

$$V_T = F\left(V_0, s, m_p, \rho_a, \alpha_0, v_w, D_P, L, l_B, l_C, l_O, C_{D0}\right), \quad (9)$$

where V_0 is the muzzle velocity, s is the distance to the target, m_p is the projectile mass, ρ_a represents air density, α_0 is the firing angle, and the v_w is the cross-wind speed.

To reduce the number of variables, a separate analysis was conducted under exemplary conditions. For an 8 g projectile, a muzzle velocity of 900 m/s was chosen as an achievable value with modern small-arms technologies. The required distance to target in terminal velocity estimations was set to 300 meters. To evaluate projectile performance under a worst-case scenario (maximum engagement distance), trajectory calculations were also conducted for 300 m. The firing angle was defined to ensure that the projectile trajectory did not exceed a maximum vertical displacement (vortex coordinate) of 0.5 m, corresponding to a point-blank trajectory for a 0.5 m high target. For the specified muzzle velocity and projectile mass, this condition resulted in a firing angle of 0.2°. Air density was set at 1.225 kg/m^3, and windless conditions were assumed to satisfy the two-dimensional assumptions of the numerical twin model. The projectile diameter, set at 7 mm in the initial experimental plan, was treated as constant.

The remaining geometric parameters of overall projectile length and the lengths of individual geometric sections were treated as variables within the ranges defined in Section 2.4.1. The fourth variable, the drag coefficient, was approximated using equation (7).

As a result of variable analysis, the input ranges for the approximation function are summarized in Table 8.

Table 8
Terminal velocity function parameters

Variable	Unit	Value
V_0	m/s	900
s	m	300
m_p	g	8.0
ρ_a	kg/m^3	1.225
α_0	deg.	0.2
v_w	m/s	0
D	mm	7.0
L	mm	30÷36
l_B	mm	3.5÷7.0
l_C	mm	8.0÷16.5
l_O	mm	16.0÷24.5

After executing the second experimental plan, which employed a Hartley design for three factors, the following results were obtained (see Table 9).

Table 9
Hartley plan PS/DS-P:Ha3 and the results of trajectory modelling for V_T

Plan							V_T
	Coded factors			Uncoded factors			
n	X_2	X_3	X_4	$x2$	$x3$	$x4$	z
1	–1	–1	1	31.268	4.240	22.704	744
2	1	–1	–1	34.732	4.240	17.796	726
3	–1	1	–1	31.268	6.260	17.796	729
4	1	1	1	34.732	6.260	22.704	749
5	–1.732	0	0	30.000	5.250	20.250	738
6	1.732	0	0	36.000	5.250	20.250	739
7	0	–1.732	0	33.000	3.500	20.250	735
8	0	1.732	0	33.000	7.000	20.250	742
9	0	0	–1.732	33.000	5.250	16.000	718
10	0	0	1.732	33.000	5.250	24.500	750
11	0	0	0	33.000	5.250	20.250	739

The second Hartley plan for three variables consists of a core set (first 4 runs), axial, or star points (runs 5–9, star arm $\alpha = 1.732$, and a central point (run 11). Simulations were conducted for each of 11 cases, with the CFD-DOE PMT solver in MATLAB.

The objective function extracted from the results shown in Table 9 was established:

$$V_T = 738.97 + 0.42X_2 + 1.84X_3 + 9.45X_4 - 0.20X_2^2 - 0.20X_3^2 - 1.66X_4^2 . \quad (10)$$

The coefficients for each factor indicate that, for the chosen projectile design and its velocity at 300 meters, the ogive length (X_4) exerts the strongest influence on the bullet performance. This aligns with the analysis of the coefficient for the objective function approximating the drag coefficient – see (7). Consequently, this geometric parameter should be the primary focus when seeking to optimize the bullet shape for improved terminal ballistics.

The adequacy of the quadratic approximation was further confirmed with a correlation coefficient of $R = 0.998$, which fulfills the requirement of the correlation factor over 0.99 stated earlier. The coefficient of determination R^2 equals 0.996, indicating excellent adequacy. Table 10 shows representative terminal velocity estimates for three selected cases, in which the bullet overall length ($x2$), boattail length ($x3$), and ogive length ($x4$) were set to randomly specified values.

The experimental plan results indicate a strong correlation between the numerically calculated projectile velocity at 300 meters and the values estimated using the approximation function. The squared error, on the order of 10^{-3} or lower, is considered acceptable for practical terminal ballistics performance assessments.

Table 10
Exemplary objective function approximation results

Parameter	Value		
Projectile overall length $x2$	34.732	30.000	36.000
Boattail length $x3$	6.260	5.250	5.250
Ogive length $x4$	22.704	20.250	20.250
C_{D0}	728.810	748.690	737.630
C_{D0} approx.	728.875	748.632	737.629
Square error	0.0042219	0.0033083	0.0000017

3.3.2. Shape optimization procedure

Regarding the maximum terminal velocity for given initial conditions, projectile shape optimization can be achieved by finding the maximum of the objective function (10). To do so, the partial derivatives of the function with respect to each factor were defined:

$$\frac{\partial V_T}{\partial X_2} = 0.42 - 0.40X_2 ,$$
$$\frac{\partial V_T}{\partial X_3} = 1.84 - 0.40X_3 ,$$
$$\frac{\partial V_T}{\partial X_4} = 9.45 - 3.32X_4 .$$

By equating the partial derivatives to zero, the stationary point at $X_2 = 1.05$, $X_3 = 4.60$, and $X_4 = 2.846$ was obtained. Since the coefficients of the quadratic terms in (10) are negative, these values correspond to the location of the maximum of the response V_T. However, the values of X_3 and X_4 exceed the upper boundary of the experimental range, which is 1.732. Therefore, the maximum response within the defined experimental region occurs at $X_3 = 1.732$ ($x3 = 7.000$ mm), $X_4 = 1.732$ ($x4 = 24.500$ mm), while the value of factor X_2 remains as calculated ($x2 = 33.649$ mm). The maximum value of terminal velocity, within the specified factor ranges, is 753.17 m/s. It must be emphasized that this value is strictly theoretical, as the condition of bearing surface length is not satisfied.

Function shown in (10) can be utilized to identify the projectile external geometry that yields the highest terminal velocity when specific constraints are placed on the projectile external shape, e.g., due to technological process, and can implement the requirement of a minimum cylindrical length, which was specified earlier. Such a tool can then be employed to evaluate how variations in the remaining geometric factors influence the terminal velocity.

Figure 11 presents the results of exemplary analysis where the terminal velocity change was analyzed for a fixed overall and boattail length and varied ogive (and therefore cylindrical part) length, while Fig. 12 shows the case with only the boattail length held constant.

By examining how each factor affects the terminal velocity of the projectile, the impact of geometric modifications can be readily evaluated. For instance, Fig. 11 illustrates that, with a

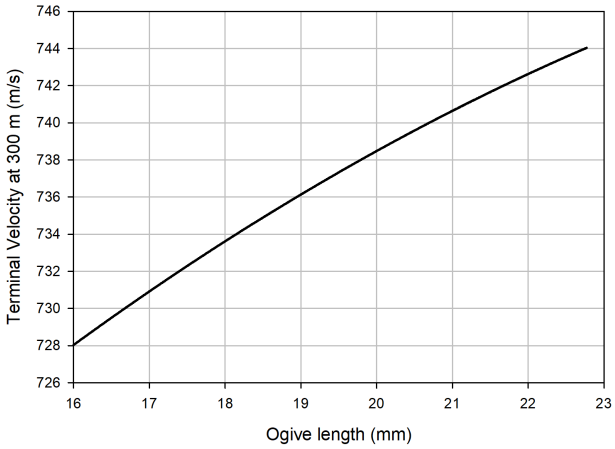

Fig. 11. Estimated terminal velocity for fixed overall and boattail lengths

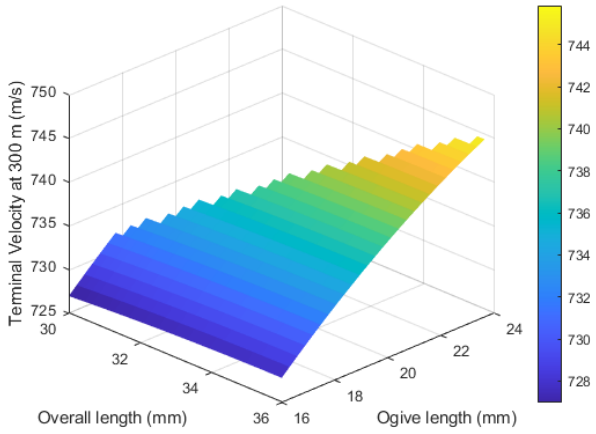

Fig. 12. Estimated terminal velocity for fixed boattail length

fixed overall length and boattail length, extending only the ogive length from 16 mm enables assessment of how much additional velocity at the target can be gained per millimeter of ogive extension (and bearing surface reduction), thereby offering direct insight into improvements in terminal ballistics performance. When greater geometry alternations are possible, the analysis shown for an exemplary set of values in Fig. 12 allows for a quick estimation of how the ogive – overall lengths trade-off – affects the terminal velocity at the chosen range. The ability to assess how much velocity at the target can be increased by slightly modifying projectile shape is especially crucial when analyzing projectile-target interaction near the ballistic limit (V50). Even a minor increase in terminal velocity near V50 can significantly affect penetration success, showing the possible advantages of using the presented methodology [11, 53].

4. CONCLUSIONS

1. CFD simulations enable the development of a numerical twin for the exterior ballistics of small-arms projectiles in supersonic flight, providing better agreement with experimental data than semi-empirical PRODAS predictions.
2. The CFD model, utilizing the k-ω SST turbulence model in Ansys Fluent, showed around 6.5% deviation when validated against experimental and literature data for supersonic projectile flow at the analyzed Mach number, confirming mesh independence.
3. The DOE approach proved to be remarkably effective in organizing and analyzing the results of experiments performed using the numerical twin, and it provided valuable results.
4. A Hartley experimental plan established strong correlations ($R > 0.99$, $R^2 > 0.98$) between Ma, geometric factors, and the drag coefficient, enabling the derivation of a highly accurate quadratic approximation function. This function was then integrated into a PMT solver for efficient trajectory simulations. The CFD-DOE PMT method proved more reliable than semi-empirical software like PRODAS, which tends to underestimate drag.
5. A second DOE plan successfully generated a quadratic function linking projectile geometry to terminal velocity at 300 meters, with extremely high adequacy ($R > 0.99$, $R^2 > 0.99$). Both functions revealed ogive length as the strongest influencing factor on drag coefficient and impact velocity. The function was directly used to find an optimal projectile shape, achieving a terminal velocity of over 753 m/s at 300 m.
6. The developed CFD-DOE PMT model is flexible and scalable, enabling adaptation to various projectile geometries and parameter ranges. The objective functions can be recalibrated through repetition of the DOE plan for new configurations or performance criteria.
7. This methodology is especially effective in analyzing terminal ballistics near the ballistic limit V50. It provides valuable insights into how small geometric modifications influence performance at a given range, helping optimize penetration potential without extensive physical prototyping.
8. The coupled approach significantly reduces development time and costs, while improving the reliability of trajectory predictions by incorporating CFD-based aerodynamic data directly into performance simulations.
9. Limitations of the approach include simplifications employed in the numerical twin construction, such as assuming axisymmetry and zero-yaw flight in the CFD model, and the assumption of maintaining constant mass of the projectile while modifying its external geometry. These factors may influence accuracy in predicting drag and stability and affect internal and terminal ballistics.
10. Experimental firing tests are planned to verify the numerical predictions of the optimized configurations and to assess the practical applicability of the CFD-DOE PMT methodology.

ACKNOWLEDGEMENTS

This work was financed by the Military University of Technology under the research project UGB 531-000049-W200-22.

REFERENCES

[1] C.F.J. Wu and M.S. Hamada, *Experiments: planning, analysis, and optimization*, USA: Wiley-Interscience, 2009.

[2] R.L. McCoy, *Modern exterior ballistics the launch and flight dynamics of symmetric projectiles*, USA: Schiffer Pub, 2009.

[3] D.E. Carlucci and S. Jacobson, *Ballistics: Theory and design of guns and ammunition*, USA: Taylor & Francis, 2018.

[4] S.I. Silton, "Navier-Stokes computations for a spinning projectile from subsonic to supersonic speeds," *J. Spacecr. Rockets*, vol. 3, no. 803, pp. 223–231, 2002, doi: 10.2514/1.4175.

[5] S.I. Silton, "Navier-Stokes predictions of aerodynamic coefficients and dynamic derivatives of a 0.50-cal projectile," in 29th *AIAA Applied Aerodynamics Conference*, 2011, doi: 10.2514/6.2011-3030.

[6] J. DeSpirito and K. Heavey, "CFD computation of magnus moment and roll-damping moment of a spinning projectile," in *AIAA Atm. Flight Mech. Conf. and Exhibit*, 2004, doi: 10.2514/6.2004-4713.

[7] J. DeSpirito and P. Plostins, "CFD prediction of M910 projectile aerodynamics: unsteady wake effect on magnus moment" in *AIAA Atmospheric Flight Mechanics Conference and Exhibit AIAA 2007-6580*, 2007, doi: 10.2514/6.2007-6580.

[8] J. DeSpirito, S.I. Silton, and P. Weinacht, "Navier-Stokes predictions of dynamic stability derivatives: evaluation of steady-state methods," *J. Spacecr. Rockets,* vol. 46, no. 44, pp. 1142–1154, 2008, doi: 10.2514/1.38666.

[9] J. Sahu, "Time-accurate numerical prediction of free flight aerodynamics of projectiles" in *2006 HPCMP Users Group Conference*, pp. 66–72, 2006, doi: 10.1109/HPCMP-UGC.2006.72.

[10] J. Kokes, M. Costello, and J. Sahu, "Generating an aerodynamic model for projectile flight simulation using unsteady, time accurate computational fluid dynamic results", *WIT Trans. Modell. Simul.,* vol. 45, no. 34, 2006, doi: 10.2495/CBAL070041.

[11] F. Simon *et al*., "Numerical simulation of magnus force control for projectiles configurations," *Comput. Fluids*, vol. 38, no. 4, pp. 965–968, 2009, doi: 10.1016/j.compfluid.2008.09.006.

[12] T. Šabanović, "Analysis of the influence of 5.56 mm projectile shape on drag coefficient using CFD," *Defense Secur. Stud*., vol. 2, pp. 79–85, 2021, doi: 10.37868/dss.v2.id172.

[13] A. Ko *et al.,* "Prediction and analysis of the aerodynamic characteristics of a spinning projectile based on computational fluid dynamics," *J. Aerosp. Eng.*, vol. 2020, p. 6043721, 2020, doi: 10.1155/2020/6043721.

[14] H. Demir *et al*, "Computational fluid dynamics analysis of drag reduction in bullet via geometric modifications," *Bayburt Üniversitesi Fen Bilimleri Dergisi*, vol. 7, pp. 47–56, 2024, doi: 10.55117/bufbd.1493857.

[15] S.I. Silton and P. Weinacht, "Effect of rifling grooves on the performance of small-caliber ammunition," U.S. Army Research Laboratory Aberdeen Proving Ground, MD, 2008.

[16] R. Sedney, "Review of base drag," US Army BRL Report 1337, Aberdeen Proving Ground, MD, 1966.

[17] J. Sahu, C.J. Nietubicz, and J.L. Steger, "Numerical computation of base flow for a projectile at transonic speeds," in *9th Atmospheric Flight Mechanics Conference*, 1982, doi: 10.2514/6.1982-1358.

[18] S. Serdarevic-Kadic and J. Terzic, "Effects of base shape to drag at transonic and supersonic speeds by CFD," *DAAAM International Scientific Book,* 2019, pp. 71–80 doi: 10.2507/daaam. scibook.2019.06.

[19] M.A. Suliman *et al.*, "Computational investigation of base drag reduction for a projectile at different flight regimes," in 13th *International Conference on Aerospace Sciences & Aviation Technology, ASAT-13*, 2009.

[20] S.C On *et al.*, "Computational drag and magnus force reduction for a transonic spinning projectile using passive porosity," *Comput. Methods Appl. Mech. Eng*., vol. 190, pp. 6125–6139, 2001, doi: 10.1016/S0045-7825(01)00210-9.

[21] S.M. Liang and J.K. Fu, "Passive control method for drag reduction for transonic projectiles," in 9th *Applied Aerodynamics Conference, 1991,* doi: 10.2514/6.1991-3213.

[22] J.-K Fu and S.M. Liang, "A numerical study of optimal drag reduction for turbulent transonic projectiles using a passive control," *Int. J. Comput. Fluid Dyn*., vol. 3, pp. 251–264, 1994, doi: 10.1080/10618569408904510.

[23] J. Lopera, T. Ng, and M. Patel, "Effects of forebody geometry on the flow and control of a blunt-nose projectile at high angles of attack," *AIAA 2007-461. 45th AIAA Aerospace Sciences Meeting and Exhibit.*, 2007, doi: 10.2514/6.2007-461.

[24] V.R. Muruganantham and T. Babin, "Numerical investigation of hybrid blend design target bullets," *MATEC Web Conf*., vol. 172, p. 01006, 2018, doi: 10.1051/matecconf/201817201006.

[25] K. Piasta, P. Kupidura, and J. Michalski. "Computational evaluation of assembly technique influence on ballistic performance of a bullet – non-linear relation between méplat size and the drag coefficient," *Technologia i Automatyzacja Montażu,* vol. 120, pp. 11–18, 2023, doi: 10.7862/tiam.2023.2.2.

[26] K. Piasta, P. Kupidura, J. Michalski, and B. Fikus, "Validation of steady-state CFD simulations for drag coefficient estimation of the 5.56×45 mm NATO cartridge using experimental methods," *J. Phys.-Conf. Ser.*, vol. 3027, p. 012048, 2025, doi: 10.1088/1742-6596/3027/1/012048.

[27] M. Morawski, B. Fikus, R. Woźniak, and R. Trębiński, "Application of design of experimental methods in theoretical analysis of the gas-delayed blowback operation firearm action," *Appl. Sci*., vol. 12, p. 12216, 2022, doi: 10.3390/app122312216.

[28] S.Y. Oh *et al.*, "Magnus and spin-damping measurements of a spinning projectile using design of experiments," *J. Spacecr. Rockets* vol. 47, pp. 974–980, 2010, doi: 10.2514/1.50188.

[29] L. Fowler and J. Rogers, "Airframe performance optimization of guided projectiles using design of experiments," *J. Spacecr. Rockets* vol. 52, pp. 1603–1613, 2015, doi: 10.2514/1.A33367.

[30] J.G. Wang *et al.*, "Numerical simulation and optimized design of cased telescoped ammunition interior ballistic," *Defence Technol.,* vol. 14, pp. 110–125, 2017, doi: 10.1016/j.dt.2017.11.006.

[31] M. Zeidler, T. Lamy, and M. Bescond, "Single and multi-objective optimization of the aerodynamics of projectiles using genetic algorithms," in *34th International Symposium on Ballistics,* 2025, doi: 10.12783/ballistics25/37177.

[32] B. Kneubuehl, "Optimization of boattails for small arms bullets," Swiss Federal Department of Defence, vol. 23, 1983.

[33] ANSYS, *ANSYS Fluent Theory Guide*, USA: Ansys Inc.

[34] G.K. Batchelor, *An introduction to fluid dynamics*, UK: Cambridge Univ. Press. 1967.

[35] S.I. Sidra and B.E. Howell, "Aerodynamic and flight dynamic characteristics of 5.56-mm ammunition: M855," Report ARL-TR-5182, 2010.

[36] M. Tutar and A.E. Holdø, "Computational modelling of flow around a circular cylinder in sub-critical flow regime with various turbulence models," *Int. J. Numer. Methods Fluids,*

vol. 35, pp. 763–784, 2001, doi: 10.1002/1097-0363(20010415)35:7<763::AID-FLD112>3.0.CO;2-S.

[37] D. Rodriguez, *Applied computational fluid dynamics and turbulence modeling: practical tools, tips and techniques*, USA: Springer Nature, 2019, p. 238.

[38] G.S. Settles, *Schlieren and shadowgraph techniques, visualizing phenomena in transparent media*. USA: Springer, 2001, pp. 28–38, doi: 10.1007/978-3-642-56640-0.

[39] M. Van Dyke, *An album of fluid motion,* USA: The Parabolic Press, 1982, pp. 154-168.

[40] A. Sasoh, *Compressible fluid dynamics and shock waves*, USA: Springer Nature, 2020, pp. 143–44, doi: 10.1007/978-981-15-0504-1.

[41] NASA EP-89, appendix F.

[42] R. Cummings, T. Yang, and Y. Oh, "Supersonic, turbulent flow computation and drag optimization for axisymmetric afterbodies," *Comput. Fluids*, vol. 24, pp. 487–507, 1995, doi: 10.1016/0045-7930(94)00040-6.

[43] B. Fikus, D. Goździk, and J. Kijewski, "Preliminary comparative investigations on ballistic properties of intermediate cartridges," *Probl. Mechatron. Armament Aviat. Saf. Eng.*, vol. 11, pp. 27–44, 2020, doi: 10.5604/01.3001.0014.5641.

[44] Arrow Tech Associate, *PRODAS version 3 technical manual*, USA: Arrow Tech Associate, 2002.

[45] K. Piasta and P. Kupidura, "Perspective armour-piercing intermediate cartridge projectile," *Probl. Mechatron. Armament Aviat. Saf. Eng.*, vol. 14, pp. 89–104, 2023, doi: 10.5604/01.3001.0016.2961.

[46] K. Piasta, J. Michalski, B. Fikus and P. Kupidura, "Projectile seating depth influence on a small arms cartridge performance," *Assem. Tech. Technol.*, vol. 124, pp. 11–17, 2024, doi: 10.7862/tiam.2024.2.2.

[47] T. Grzegorczyk, J. Janiszewski and R. Trębiński, *Metrologia i teoria eksperymentu*, II. Warszawa: WAT, S-59928. (in Polish)

[48] J. Antony. *Design of experiments for engineers and scientists*. UK: Butterworth–Heinemann, 2003.

[49] J. Sacks, W.J. Welch, T.J. Mitchell, and H.P. Wynn, "Design and analysis of computer experiments," *Statist. Sci.,* vol. 4, pp. 409–435, 1989, doi: 10.1214/ss/1177012413.

[50] R. Myers, D. Montgomery and C. Anderson-Cook, *Response surface methodology: process and product optimization using designed experiments*, USA: Wiley, 2009.

[51] M.K. Alkharisi and H.A. Dahis, "The application of response surface methodology and machine learning for predicting the compressive strength of recycled aggregate concrete containing polypropylene fibers and supplementary cementitious materials," *Sustainability,* vol. 17, p. 2913, 2024, doi: 10.3390/su17072913.

[52] M.M. Aziz *et al.*, "Numerical simulations and drag prediction for base bleed projectile," *J. Multidiscip. Eng. Sci. Technol.,* vol. 7, pp. 12717–12722, 2020.

[53] Z. Rosenberg and E. Dekel, *Terminal ballistics*, USA: Springer, 2012, doi: 10.1007/978-3-642-30488-0.